

Payload Grasping and Transportation by a Quadrotor with a Hook-Based Manipulator

Péter Antal, Tamás Péni, and Roland Tóth ^{*†}

Abstract

The paper proposes an efficient trajectory planning and control approach for payload grasping and transportation using an aerial manipulator. The proposed manipulator structure consists of a hook attached to a quadrotor using a 1 DoF revolute joint. To perform payload grasping, transportation, and release, first, time-optimal reference trajectories are designed through specific waypoints to ensure the fast and reliable execution of the tasks. Then, a two-stage motion control approach is developed based on a robust geometric controller for precise and reliable reference tracking and a linear–quadratic payload regulator for rapid setpoint stabilization of the payload swing. The proposed control architecture and design are evaluated in a high-fidelity physical simulator with external disturbances and also in real flight experiments.

I. INTRODUCTION

The aim of this work is to develop and implement efficient trajectory planning and control methods for payload grasping and transportation using a quadrotor-based aerial manipulator. Our work is motivated by current industrial developments, where drones are used to solve autonomous transportation tasks, e.g. for building construction, military purposes or assistance in manufacturing by transporting parts between production cells [1]. In these applications, a gripping mechanism is required that is simple, easy to use, and connects the payload to the drone without human interaction.

In the literature of transportation with quadcopters, the payload is usually connected to the quadrotor via flexible cables that are attached manually before the drone takes off [2, 3]. Cable suspension has several advantages, for example the differential flatness property of the coupled system can be exploited to simplify planning dynamically feasible, smooth trajectories [4, 5]. Other advantages include good maneuverability, simple mechanical structure, and ability to apply multiple vehicles to collaboratively transport a heavy

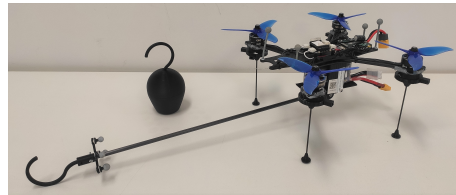


Fig. 1: Quadrotor with a hook-based manipulator.

payload. However, the physical modelling of rope tension is complex, and the large number of degrees of freedom makes precise positioning challenging.

Aerial manipulation and grasping using robotic extensions is also a popular field of research [6]. In [7], the dynamic model and Cartesian impedance control of a UAV equipped with a robotic arm is proposed. In [8], autonomous grasping is proposed with robotic claws, inspired by how predatory birds grasp their prey. In [2], magnetic grippers are used to transport a cable-suspended load with two quadrotors. In [9], a custom designed gripper is proposed specifically for grasping and carrying foam elements. The main advantage of robotic arms and grippers is that they are actuated, which makes gripping possible even in the presence of small positioning errors. However, most of them are designed specifically for one task, specific material, or payload, therefore their scalability and general applicability is questionable.

Motivated by the presented industrial and research challenges, we propose a grasping mechanism which consists of a hook fixed to a rigid rod, which is connected to a quadrotor by an unactuated 1 DoF revolute joint. Using this quadrotor–hook manipulator system, we intend to move objects by picking them up and putting them down precisely at pre-specified locations, within minimal time. Each object is assumed to have a hook attached on top which makes the grasping possible. The advantages of our setup compared to the previously introduced configurations are as follows. First, the applied pole is more rigid than flexible cables and only has one degree of freedom, which decreases the complexity of precise positioning and makes modelling the cable tension unnecessary. Second, the gripping mechanism is not actuated in any form, resulting in a simple, light-weight and cheap mechanical design. Moreover, the solution is also scalable: by equipping a heavy payload with hooks, it can be transported using multiple vehicles collaboratively.

Besides the operational advantages brought by the proposed gripper mechanism, it also induces major challenges

^{*}This research was supported by the European Union within the framework of the National Laboratory for Autonomous Systems (RRF-2.3.1-21-2022-00002) and by the Eötvös Loránd Research Network (grant. number: SA-77/2021).

[†]The authors are with the Systems and Control Laboratory, Institute for Computer Science and Control, Budapest, Hungary (email: antalpet@szlaki.hu, peni@szlaki.hu, tothroland@szlaki.hu). R. Tóth is also affiliated with the Control Systems Group of the Eindhoven University of Technology.

in modelling and control. To attach and detach the hooks, advanced planning and precise positioning are required, because large tracking errors can lead to unsuccessful grasping and even instability of the load attached system. Moreover, the impact behaviour and the friction between the gripper and the hook is difficult to model realistically.

To address the introduced challenges, the contributions of this work are as follows:

1. We propose a novel path planning solution for hook based transportation: the reference trajectory is constructed based on 5 segments, each designed using a minimal time planning method inspired by [10].
2. We derive an extension of the nonlinear robust geometric controller originally suggested in [11] to achieve precise and reliable tracking of fast, agile trajectories even in the presence of external disturbances. To compensate the effect of the transported payload, we augment the control law with a feedforward term.
3. To rapidly damp the swing of the payload and ensure precise release at the target location, we propose a linear–quadratic payload regulator designed for the planar model of the quadrotor–hook manipulator.
4. We optimize the parameters and evaluate the performance of the proposed algorithms by constructing real-world scenarios with realistic external disturbances in MuJoCo, a high-fidelity physical simulator [12].
5. We evaluate the performance of the proposed methods in real flight experiments using a self-developed aerial manipulator platform.

This work is organized as follows. First, we introduce the dynamic model of the mechanism in Section II. In Sections III and IV, we describe the proposed trajectory planning and control methods, respectively. In Sections V and VI, we analyze the performance of the proposed methods in high-fidelity physical simulations, and also in real-world flight experiments. Finally, in Section VII, we draw conclusions on the proposed method and the achieved results.

II. MODELLING

A. Quadrotor Dynamics

In this subsection, the dynamic model of the quadrotor without the hook is derived. The vehicle is modelled as a rigid body in 3D space affected by the gravitational force and the rotation of the propellers. Using the inertial frame (\mathcal{F}^i) and the body frame (\mathcal{F}^b) illustrated in Fig. 2, the motion of the quadcopter is governed by the following equations:

$$m\ddot{r} = -mge_3 + FRe_3, \quad (1a)$$

$$J\dot{\omega} = \tau - \omega \times J\omega, \quad (1b)$$

$$\dot{R} = R\hat{\omega}, \quad (1c)$$

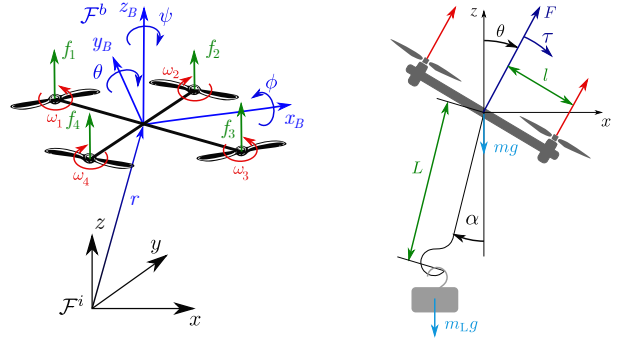


Fig. 2: Left: inertial and body frames describing the geometric relations of the quadcopter and the environment. Right: free body diagram of the manipulator in the vertical plane.

where $r \in \mathbb{R}^3$ is the position of the drone, and $R \in \text{SO}(3)$ is the rotation matrix from \mathcal{F}^b to \mathcal{F}^i , where $\text{SO}(3)$ denotes the special orthogonal group, also called the *rotation group*. Moreover, $\omega \in \mathbb{R}^3$ is the angular velocity in \mathcal{F}^b , m is the mass of the drone, J is the inertia matrix in \mathcal{F}^b , g is the gravitational acceleration, and e_3 is the unit vector of the z axis in \mathcal{F}^i . The notation $\hat{\cdot}$ stands for the projection: $\mathbb{R}^3 \rightarrow \text{SO}(3)$ ensuring that $\hat{x}\hat{y} = x \times y$ for all $x, y \in \mathbb{R}^3$ where \times corresponds to the vector product. Beside of R , we also use the Euler angles (roll: ϕ , pitch: θ , yaw: ψ) to characterize the rotation from \mathcal{F}^b to \mathcal{F}^i , as it is illustrated in Fig. 2. The inputs of the system are the collective thrust F and the torque vector $\tau = [\tau_x \tau_y \tau_z]^\top$ [13].

The dynamic model of the quadcopter is underactuated as it has 6 DoFs but only 4 control inputs. However, in trajectory design, we exploit that the model is *differentially flat* [13], i.e., all state variables and control inputs can be expressed from a finite number of time derivatives of the *flat outputs*, namely the position x, y, z and yaw angle ψ . This simplifies the trajectory planning as all other states depend on $x_d(t), y_d(t), z_d(t), \psi_d(t)$, therefore only these trajectories have to be constructed instead of considering the full state. Moreover, utilizing differential flatness resolves underactuation, because the reference trajectories designed for the flat outputs are inherently dynamically feasible.

B. Manipulator Dynamics

The proposed control design exploits the manipulator dynamics only at a specific case where the roll (ϕ) and yaw (ψ) angles are assumed to be zero. This results in a simplified model of 4 degrees of freedom and 2 control inputs. We choose the payload position $[x_L \ z_L]^\top$, the quadrotor pitch θ , and the swing angle α to characterize the dynamic equations, because we intend to control these variables directly to rapidly damp the swing of the payload. By applying the Newton-Euler equations and using the free body diagram in Fig. 2, we are able

to formulate the equations of motion as follows:

$$\begin{bmatrix} \ddot{x}_L \\ \ddot{z}_L \end{bmatrix} = \begin{bmatrix} 0 \\ -g \end{bmatrix} + \frac{F \cos(\theta - \alpha) + mL\dot{\alpha}^2}{m + m_L} \begin{bmatrix} \sin \alpha \\ \cos \alpha \end{bmatrix}, \quad (2a)$$

$$mL\ddot{\alpha} = F \sin(\theta - \alpha), \quad (2b)$$

$$J_y \ddot{\theta} = \tau_y, \quad (2c)$$

where m_L is the mass of the payload, J_y is the inertia of the quadrotor in the (x, z) plane, and L is the pole length.

III. MOTION TRAJECTORY PLANNING

A. Overall concept

To perform successful payload grasping and transportation, we propose a motion sequence for the aerial manipulator consisting of 5 segments:

1. Reach the plane of the payload with the quadrotor
2. Approach the payload and attach the hook
3. Take the payload to the target position
4. Release the payload
5. Detach the hook

The trajectory segments are depicted in Fig. 3 with waypoints A, B, C, D, E, F describing the connection points between the segments and the plane P , which is spanned by the normal vector of the hook on the payload (n_{hook}), and the z axis of the world frame. The position of the waypoints A, C, D, E, F are fixed based on the initial and the intended final configuration of the quadrotor and the payload, while the position of waypoint B is determined by the solution of the trajectory optimization.

In trajectory planning, we neglect the dynamics introduced by the 1 DoF hook attachment and consider it as a rigid attachment with $\alpha \equiv 0$. Consequently, we design reference trajectories for the flat outputs of the quadrotor system derived in Sec. A, namely the position and yaw angle, the rest of the states in terms of roll and pitch and their velocities will be completely determined through the kinematic relations. Then, the swing of the hook and the payload are compensated by controller design (detailed in Section IV).

B. Spatial (x, y, z) trajectory

For the position, each segment is designed in two steps, based on an indirect time optimal trajectory planning method inspired by [10]. First, we design a spatial trajectory $r_d(s)$ as a function of the path variable s , and then we construct a velocity profile by determining the time dependence of s . We represent the spatial trajectory by B-spline curves defined by their basis functions and coefficients, as follows:

$$r_d(s) = \begin{bmatrix} x_d(s) \\ y_d(s) \\ z_d(s) \end{bmatrix} = [c_x \quad c_y \quad c_z]^\top \vartheta(s) = c^\top \vartheta(s), \quad (3)$$

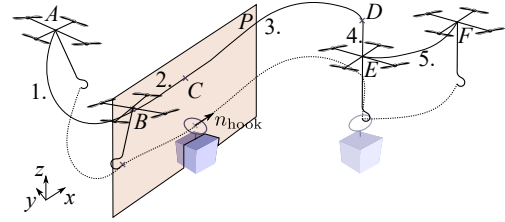


Fig. 3: Motion trajectory segments and waypoints.

where $\vartheta : \mathbb{R} \rightarrow \mathbb{R}^{n_c}$ is the B-spline basis of degree n_r , $c \in \mathbb{R}^{n_c \times 3}$ is the coefficient matrix, and $s \in [0, 1]$ is the parameter of the B-spline curve. This formulation ensures that the designed path is $n_r - 2$ times continuously differentiable given the knots of the B-splines are distinct. Furthermore, the B-spline and its derivatives are linear in the coefficients allowing us to formulate trajectory optimization as a quadratic problem with linear constraints.

For the spatial trajectory, we minimize the jerk and the arc length of the curves by constructing the objective function as follows [14]:

$$J_{\text{jerk}} = \sum_{f \in \{x_d, y_d, z_d\}} \int_0^1 \left(\frac{d^3 f(s)}{ds^3} \right)^2 ds, \quad (4a)$$

$$J_{\text{length}} = \int_0^1 \sqrt{(x'_d(s))^2 + (y'_d(s))^2 + (z'_d(s))^2} ds, \quad (4b)$$

$$J = w J_{\text{jerk}} + (1 - w) J_{\text{length}}^2, \quad w \in [0, 1], \quad (4c)$$

where w is a trade-off parameter chosen by the user. Throughout this work, $g'(s)$ denotes the derivative of function g with respect to (w.r.t.) the parameter s , and $\dot{g}(s(t))$ denotes the derivative of g w.r.t. time: $\dot{g}(s(t)) = g'(s(t))\dot{s}(t)$.

In order to incorporate the waypoints illustrated in Fig. 3, we prescribe boundary conditions on the spatial trajectory and also on its derivatives. This leads to a quadratic optimization problem of the coefficients of the spatial trajectory:

$$\begin{aligned} \tilde{c}^* &= \arg \min J(\tilde{c}), \\ \text{subject to } & A\tilde{c} = b, \\ & G\tilde{c} \leq h, \end{aligned} \quad (5)$$

where $\tilde{c} = [c_x^\top \quad c_y^\top \quad c_z^\top]^\top$ and the constraints determined by A, b, G, h are discussed later in Section III-D.

C. Temporal (x, y, z) trajectory

The optimal time allocation method we employ has been proposed in [10], and applied to quadcopter trajectory planning in [14, 3]. The objective of the planning is to design the velocity profile $s(t) : \mathbb{R} \rightarrow [0, 1]$ such that it minimizes the execution time of the trajectory while satisfying motion constraints for the quadrotor. The objective of the planning is to minimize the duration of the trajectory T , which can be formulated as

$$T = \int_0^T 1 dt = \int_0^1 \frac{1}{\dot{s}} ds. \quad (6)$$

Similar to [14], we also incorporate the actuation constraints in the objective by penalizing the acceleration along the path, as the control inputs of the quadrotor appear at the acceleration level in the dynamic model characterized by (1). Given that the spatial path $r_d(s)$ is already designed based on (5), the constrained optimal time allocation problem is formulated as follows:

$$\begin{aligned} \underset{s(t)}{\text{minimize}} \quad & J_T = \int_0^1 \left(\rho \dot{s}^2 + (1 - \rho) \frac{1}{\dot{s}} \right) ds \\ \text{subject to} \quad & \dot{r}_d(0) = v_0, \quad \dot{r}_d(1) = v_f, \\ & -v_{\max} \leq \dot{r}_d(s(t)) \leq v_{\max}, \\ & -a_{\max} \leq \ddot{r}_d(s(t)) \leq a_{\max}, \\ & -\lambda_{\max} \leq \lambda(s(t)) \leq \lambda_{\max}, \\ & \dot{s}(t) \geq 0, \quad t \in [0, T], \end{aligned} \quad (7)$$

where $\rho \in [0, 1]$ is a tradeoff parameter, and $\lambda(s(t))$ is the rate of the acceleration (similar to jerk, but differentiated w.r.t the path variable s [14]). The initial and final velocity $v_0, v_f \in \mathbb{R}^3$ ensure the continuity of the trajectory segments, and the inequality constraints guarantee that the velocity, acceleration, and acceleration rate remain within their allowed range. The bounds $v_{\max}, a_{\max}, \lambda_{\max} \in \mathbb{R}^3$ depend on the specific quadrotor configuration, we treat them as hyperparameters and we give an optimization based approach to choose their values in Section III-F.

Optimization (7) is nonlinear and complicated to solve in this form. However, by the direct transcription method introduced in [10], it can be reformulated as a *second-order cone optimization problem* (SOCP) by discretizing the temporal trajectory over a grid of s , and assuming that \dot{s} is piecewise constant between adjacent grid points. The numerical solution of the resulting SOCP can be obtained in polynomial time by using an off-the-shelf convex solver.

D. Boundary conditions of the trajectory segments

In this section, we formulate the corresponding boundary conditions for both the spatial and temporal trajectory of each segment, depicted in Fig. 3. The segments are distinct in the sense that we construct both the spatial and temporal trajectory of a segment before moving on to the next one. From here on, we use the notation $r_{d,i}(s_i(t_i)), i \in \{1, \dots, 5\}$ for each trajectory segment, where $s_i(0) = 0, s_i(1) = 1$, and $t_i \in [0, T_i]$. To connect two successive trajectory segments, the continuity of the position and velocity are ensured by the following constraints:

$$r_{d,i+1}(0) = r_{d,i}(1), \quad \dot{r}_{d,i+1}(0) = \dot{r}_{d,i}(1). \quad (8)$$

In the first segment of the motion sequence, the aim is to reach plane P from any given initial position r_0 and velocity v_0 , therefore at point A , the following constraints are set:

$$r_{d,1}(0) = r_0, \quad \dot{r}_{d,1}(0) = v_0. \quad (9)$$

At point B , we wish to achieve a smooth transition to plane P , therefore the position is required to be within the plane

with zero velocity and acceleration perpendicular to the plane. To simplify the mathematical formulation of the constraints, w.l.o.g., we fix the object plane P to the global $x-z$ plane. In the x direction, we set the position to a safety distance from the object to ensure that the controller drives the vehicle to the plane even in the presence of small tracking errors. We also constrain the direction of the spatial trajectory to ensure that the velocity vector of the quadrotor at point B does not point in the opposite direction of the payload. In the z direction, we prescribe inequality constraints for both the position and the direction of the spatial trajectory to make the hook attach easier in the second segment. These constraints are formulated as follows:

$$\begin{aligned} y_{d,1}(1) &= 0, \quad y'_{d,1}(1) = 0, \quad y''_{d,1}(1) = 0, \\ x_{d,1}(1) &= x_B, \quad x'_{d,1}(1) \geq \partial_s x_B, \\ z_{B,\min} &\leq z_{d,1}(1) \leq z_{B,\max}, \\ \partial_s z_{B,\min} &\leq z'_{d,1}(1) \leq \partial_s z_{B,\max}, \end{aligned} \quad (10)$$

where x_B and $\partial_s x_B, z_{B,\min}, z_{B,\max}, \partial_s z_{B,\min}, \partial_s z_{B,\max}$ are hyperparameters.

At point C , we constrain the position and the direction of the spatial path to ensure safe attaching of the hook. Moreover, assuming that the swing angle is $\alpha = 0$, the following constraints are formulated:

$$\begin{aligned} r_{d,2}(1) &= r_{L,\text{init}} + Le_3, \\ x'_{d,2}(1) &\geq 0, \quad y'_{d,1}(1) = 0, \quad z'_{d,1}(1) = 0, \end{aligned} \quad (11)$$

where $r_{L,\text{init}}$ is the initial position of the payload, and e_3 is the unit vector of the z axis in the world frame.

Between points C and D , we transport the payload to be above the target position and stop there. We intend to achieve a precise release by fixing the first and second derivatives of the spatial path to zero in x and y directions:

$$r_{d,3}(1) = r_{L,\text{target}} + z_D, \quad \dot{r}_{d,3}(1) = 0, \quad (12)$$

$$x'_{d,3}(1) = y'_{d,3}(1) = x''_{d,3}(1) = y''_{d,3}(1) = 0, \quad (13)$$

where $r_{L,\text{target}}$ is the target position of the payload and z_D is a safety height, treated as a hyperparameter.

From point D to E , the quadcopter slowly descends to release the payload. As an end condition, we set the z position of the drone such that the hook is detached after the end of this segment. These constraints are written as follows:

$$r_{d,4}(1) = r_{L,\text{target}} + Le_3 - \frac{1}{2}d_h, \quad \dot{r}_{d,4}(1) = 0, \quad (14)$$

where d_h is the diameter of the hook.

Unlike all other waypoints, the spatial trajectory at point E is not continuous, segment 5 starts with horizontal direction to ensure that the hook is detached successfully and the payload stays on the ground. The position at point F (r_F) can be chosen arbitrarily by the user, the only goal of this trajectory segment is to make sure that the payload is released. The constraints of this segment are formulated as

$$r_{d,5}(1) = r_F, \quad z'_{d,5}(0) = z''_{d,5}(0) = 0. \quad (15)$$

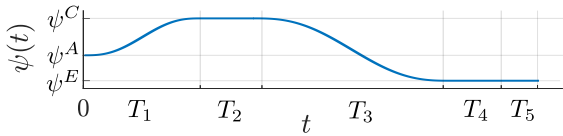


Fig. 4: Schematic trajectory of the yaw angle reference.

Finally, we incorporate the position and spatial derivative constraints into Optimization (5), moreover, the velocity and acceleration type constraints into Optimization (7). All boundary conditions are linear in the optimization variables, so they do not increase the complexity of the optimization.

E. Yaw trajectory

The yaw dynamics of a quadrotor are independent of the (x, y, z) path, therefore the yaw reference ψ_d can be freely chosen. The orientation of the hook is only restricted at points A , C , E in terms of the initial quadrotor orientation, final payload orientation and the orientation of the payload (ensuring that the hook can be attached to it), respectively.

To provide smooth transition between the specified yaw set-points, we design fifth order polynomial trajectories at Segments 1 and 3, and prescribe constant reference at the remaining segments. Given that the time duration of each segment is obtained from the solution of Optimization (7), moreover, the initial and final values of the polynomial trajectories are known, and by prescribing zero initial and final angular velocity and angular acceleration, the coefficients of the polynomial trajectories can be directly obtained from the solution of a linear equation. A schematic trajectory is depicted in Fig. 4 to illustrate the polynomial segments.

F. Hyperparameter optimization

The temporal trajectory optimization problem (7) enables us to prescribe constraints for the velocity, acceleration, and differential acceleration. However, the exact formulation of the actuator constraints would result in a set of nonlinear equations on the acceleration level and the convexity of the optimization would be lost. To address this issue, we treat the constraint bounds and the cost function weight at (4c) as hyperparameters, and propose a simple optimization program to find the best parameters that results in successful grasping and minimal execution time. By defining the hyperparameter vector as $\eta = [v_{\max} \ a_{\max} \ \lambda_{\max} \ w] \in \mathbb{R}^4$, the optimization problem is formulated as

$$\begin{aligned} \eta^* &= \arg \min_{\eta} \sum_{i=1}^5 T_i(\eta), \\ \text{subject to } r_L(T_D)^\top e_z &\geq \delta_z, \end{aligned} \quad (16)$$

where $r_L(T_D)$ is the payload position when the drone is at point D , and $\delta_z > 0$ ensures that the payload is above the ground, therefore the grasping is successful. The objective function of Optimization (16) is difficult to express in closed

Table 1: Control scheduling during payload transportation.

Segments 1-2	Segment 3	Point D	Segment 4	Segment 5
Geom. (19)	Geom. + FF (19), (21)	LQR (23)	Geom. + FF (19), (21)	Geom. (19)

form, therefore we apply a grid search to compute the solution [15]. We set the bounds of the operating domain based on physical intuition, and run simulations from several initial conditions on a grid of the parameter set. Finally, we choose the hyperparameters that minimize the total time with successful grasping. Although the numerical solution of the optimization problem is computationally demanding, it is calculated off-line and only once for a given quadrotor and hook-based manipulator configuration.

IV. MOTION CONTROL

A. Overall concept

We design a dual mode motion control approach to execute the designed trajectory and ensure successful realization of the transportation task. To follow the motion trajectory of the quadrotor in terms of reference position r_d and reference yaw angle ψ_d detailed in Section III, we treat the hook-based manipulator as an uncertainty acting on the quadrotor dynamics and employ a robust geometric control method. Moreover, to compensate the gravitational force of the payload, we augment the controller with a feedforward (FF) term that is activated after attaching the hook to the payload. However, initial results have shown that the swing of the payload can become significant during agile transportation, leading to imprecise positioning at Segment 4 of the motion. To tackle this problem, we fix the reference at point D and switch to a linear-quadratic setpoint controller to damp the payload oscillations. After a fixed time, the geometric controller is re-enabled to finish the maneuver. The scheduling of the controllers is illustrated in Table 1.

B. Nonlinear robust geometric control

For precise and reliable trajectory tracking, we use a nonlinear robust geometric controller based on [11], which is able to follow a reference trajectory in $SE(3)$ in terms of position $r_d(t) = [x_d(t) \ y_d(t) \ z_d(t)]^\top \in \mathbb{R}^3$ and orientation $R_d(t) \in SO(3)$, where $SE(3)$ denotes the special Euclidean group that comprises arbitrary translations and rotations of a rigid body in 3D space. The reference orientation $R_d(t)$ is fully determined by the reference position $r_d(t)$ and yaw angle $\psi_d(t)$. To synthesize the control law, the quadrotor dynamics are augmented by rotational and translational uncertainty terms, resulting in the set of uncertain dynamic equations:

$$m\ddot{r} = -mge_3 + FRe_3 + \Delta_r(t), \quad (17a)$$

$$J\dot{\omega} = \tau - \omega \times J\omega + \Delta_R(t), \quad (17b)$$

$$\dot{R} = R\hat{\omega}, \quad (17c)$$

where $\Delta_r(t), \Delta_R(t) \in \mathbb{R}^3$ are unstructured uncertainties. These terms represent multiple effects: parameter uncertainties (e.g. mass, inertia), unmodeled aerodynamics (e.g. blade flapping or downwash [16]), and external disturbances (e.g. strong wind). Similarly to [11], we assume that the norm of the uncertainties are bounded by

$$\|\Delta_r(t)\| \leq \delta_r, \quad \|\Delta_R(t)\| \leq \delta_R. \quad (18)$$

where $\delta_r, \delta_R \in \mathbb{R}$ are fixed constants, and $\|\cdot\|$ is the Euclidean vector norm. Force and torque inputs are computed based on the following control law:

$$F = (-k_r e_r - k_v e_v + m g e_3 + m \ddot{r}_d + \mu_r)^\top R e_3, \quad (19a)$$

$$\begin{aligned} \tau &= -k_R e_R - k_\omega e_\omega + \omega \times J \omega \\ &\quad - J(\hat{\omega} R^\top R_d \omega_d - R^\top R_d \dot{\omega}_d + \mu_R), \end{aligned} \quad (19b)$$

where $k_r, k_v, k_R, k_\omega \in \mathbb{R}$ are the control gains. The tracking errors $e_r, e_v, e_R, e_\omega \in \mathbb{R}^3$ and the robust control inputs $\mu_r, \mu_R \in \mathbb{R}^3$ are defined as follows:

$$\begin{aligned} e_r &= r - r_d, & e_v &= \dot{r} - \dot{r}_d, \\ e_R &= \frac{1}{2} (R_d^\top R - R^\top R_d)^\vee, & e_\omega &= \omega - R^\top R_d \omega_d, \\ \mu_r &= -\frac{\delta_r^{\kappa+2} e_B \|e_B\|^\kappa}{\delta_r^{\kappa+1} \|e_B\|^{\kappa+1} + \epsilon_r^{\kappa+1}}, & e_B &= e_v + \frac{c_1}{m} e_r, \\ \mu_R &= -\frac{\delta_R^2 e_A}{\delta_R \|e_A\| + \epsilon_R}, & e_A &= e_\omega + c_2 J^{-1} e_R, \end{aligned} \quad (20)$$

where $c_1, c_2, \epsilon_r, \epsilon_R, \kappa$ are positive constants, $\kappa > 2$, and the *vec operator* $(\cdot)^\vee : \text{SO}(3) \rightarrow \mathbb{R}^3$ is the inverse of the hat operator $(\hat{\cdot})$ introduced in Section II. It is proven in [11] that the tracking errors (e_r, e_v, e_R, e_ω) are uniformly ultimately bounded, using the control law (19), when the control gains are chosen according to the stability conditions in [11].

Before payload grasping, i.e., between points *A* and *C* of the trajectory illustrated in Fig. 3, we use the control law (19). However, the payload changes the mass of the system significantly, therefore we augment the controller with a feed-forward thrust to compensate for the gravitational force:

$$F_L = F + m_L g e_3^\top R e_3 = F + F_{ff}. \quad (21)$$

The resulting collective thrust given by (21) is able to compensate the vertical tracking error imposed by the transported payload, if the orientation of the quadrotor is near hovering, and the robustness of the control law mitigates additional unmodeled dynamic effects.

C. Linear-quadratic payload regulator

The geometric control introduced previously renders the quadcopter able to perform fast, agile maneuvers, however, due to high accelerations, the swing of the payload becomes significant, which makes precise positioning difficult. To address this issue, we introduce a *linear-quadratic regulator* (LQR) [17] for the setpoint stabilization of the payload.

The payload can only swing around the *y* axis of the quadcopter body frame, therefore we use the 2D model of the system described by (2) to synthesize the control law. The controller is designed for the hovering operating point with swing angle $\alpha = 0$. The local LTI dynamics are obtained from the first order Taylor approximation of the nonlinear equations of motion, as follows:

$$\dot{\xi} \approx \underbrace{\frac{\partial f(\xi, u)}{\partial \xi} \Big|_{\xi_0, u_0}}_A (\xi - \xi_0) + \underbrace{\frac{\partial f(\xi, u)}{\partial u} \Big|_{\xi_0, u_0}}_B (u - u_0), \quad (22)$$

where $\xi = [x_L \dot{x}_L z_L \dot{z}_L \theta \dot{\theta} \alpha \dot{\alpha}]^\top$, $u = [F \tau_y]^\top$, $\xi_0 = 0_{8 \times 8}$, $u_0 = [(m + m_L)g \ 0]^\top$, f is given by (2), $A \in \mathbb{R}^{8 \times 8}$ and $B \in \mathbb{R}^{8 \times 2}$. The control input provided by the LQR controller is calculated as follows:

$$u = u_0 - K(\xi - \xi_0), \quad (23)$$

where $K \in \mathbb{R}^{2 \times 8}$ is the linear feedback gain that minimizes the following cost function:

$$\int_0^\infty ((\xi - \xi_0)^\top W_Q (\xi - \xi_0) + (u - u_0)^\top W_R (u - u_0)) dt,$$

subject to (22) and (23). The state and input matrices are chosen to $W_Q = I \in \mathbb{R}^{7 \times 7}$ and $W_R = 0.01I \in \mathbb{R}^{2 \times 2}$, respectively, because we intend to control both the state and input variables with uniform weights, and we prioritize minimizing the state error over the control effort.

Note, that only F and τ_y are regulated by the LQR, the off-plane dynamics are stabilized by applying the geometric controller (19b) to compute τ_x and τ_z .

V. SIMULATION STUDY

A. Simulation environment

We analyze the proposed trajectory planning and control methods in a high-fidelity physics simulator in emulated real-world scenarios. The physical parameters of our self-developed quadrotor-hook manipulator platform are shown in Table 2. To simulate the dynamics of the resulting system, we use MuJoCo [12], an open source physics engine that makes it possible to efficiently simulate complex dynamic systems with collisions and contacts, thus facilitates model-based optimization and control design. The source code of the simulations is available at GitHub.

B. Trajectory planning

The hyperparameters of the motion planning method, namely the maximal velocity, acceleration, differential acceleration, and the weight of the cost function at (4c) are determined as the solution of Optimization (16). To find the optimal hyperparameter set, we have applied grid search with the following search interval:

$$\begin{aligned} v_{\max} &\in [0.7, 3] \text{ m/s}, & a_{\max} &\in [0.2, 2] \text{ m/s}^2, \\ \lambda_{\max} &\in [0.1, 0.8], & w &\in [0.01, 0.9], \end{aligned} \quad (24)$$

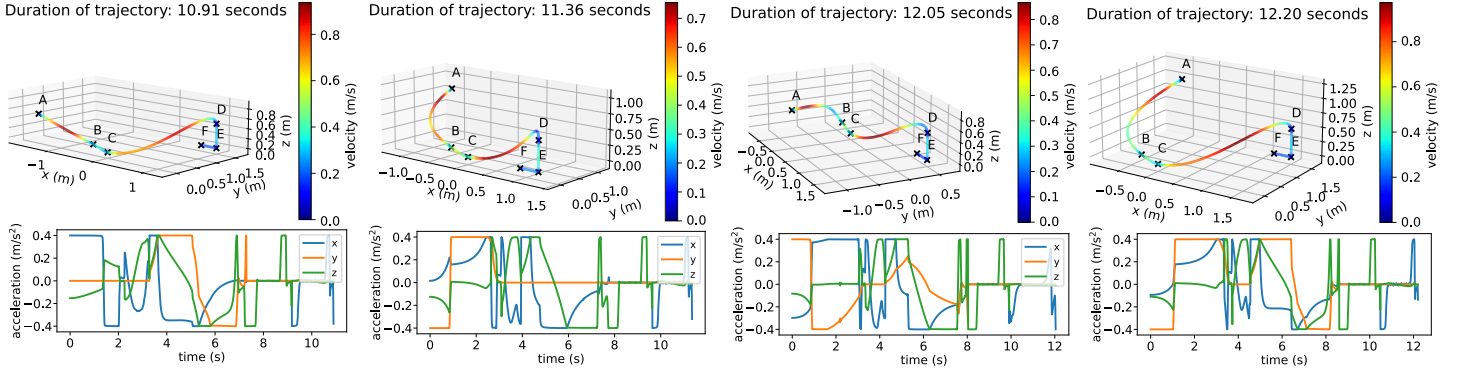


Fig. 5: Sample trajectories with the corresponding velocity profiles and accelerations in 4 test scenarios. The waypoints of the trajectory segments are labeled similarly to Fig. 3.

Table 2: Parameters of the manipulator and the geometric controller.

Drone mass	m	$6.05 \cdot 10^{-1}$	kg	k_r	4.0
x axis inertia	J_x	$1.5 \cdot 10^{-3}$	kgm ²	k_v	2.0
y axis inertia	J_y	$1.45 \cdot 10^{-3}$	kgm ²	k_R	1.7
z axis inertia	J_z	$2.66 \cdot 10^{-3}$	kgm ²	k_ω	0.2
Rotor distance	l	$8.3 \cdot 10^{-2}$	m	c_1	1.0
Pole length	L	$4.0 \cdot 10^{-1}$	m	c_2	10^{-3}
Hook mass	m_h	$1.0 \cdot 10^{-2}$	kg	ϵ_r, ϵ_R	10^{-4}
Hook diameter	d_h	$4.0 \cdot 10^{-2}$	m	κ	3

with 10 uniformly distributed values for v_{\max} , a_{\max} , λ_{\max} , and 4 values for w in terms of grid points (4000 cases). To test the feasibility and execution time of each parameter combination, we simulated 6 different scenarios of the grasping maneuver in terms of the initial and final configuration of the hook-based manipulator. The numerical values of the hyperparameters obtained from the solution of Optimization (16) are as follows:

$$\begin{aligned} v_{\max}^* &= 1.46 \text{ m/s}, & a_{\max}^* &= 0.4 \text{ m/s}^2, \\ \lambda_{\max}^* &= 0.2, & w^* &= 0.5. \end{aligned} \quad (25)$$

Beside of the optimized variables, there are other parameters, namely the degree n_r and number of coefficients n_c of the B-spline curve representing the spatial trajectory, the number of grid points K by the temporal trajectory, and the control input weight ρ in the Optimization (7). The numerical values of these parameters have been chosen based on the guidelines derived in [14] on similar trajectory optimization problems, as follows

$$n_r = 5, n_c = 12, K = 15, \rho = 0.1. \quad (26)$$

For each of the 5 segments detailed in Sec. A, a quadratic program (QP) has been constructed for the spatial trajectory, and a second-order cone program (SOCP) has been set up for the temporal trajectory. To solve these problems, we have used Mosek, a large scale, efficient optimization toolbox. On a Windows notebook with Intel i5 CPU and 8GB RAM, the average computation time of the QP is $T_{\text{QP}} = 3.30$ ms, while, for the SOCP, is $T_{\text{SOCP}} = 42.7$ ms. These values correspond to one of the five segments, therefore the full optimization time for grasping, transportation and release

is $T_{\text{opt,full}} = 5(T_{\text{QP}} + T_{\text{SOCP}}) = 230$ ms in average. However, the construction of constraint matrices and other matrix operations are computationally demanding, therefore the full computation time of a trajectory planning is significantly larger than the pure optimization times, it is $T_{\text{full}} = 1.54$ s in average. Although this computation time is already acceptable for real-world applications, it can be greatly reduced by pre-compiling the optimization problem and running the same code with different parameters when a new trajectory is needed.

The motion planning is illustrated in Fig. 5 with sample trajectories using various initial and final conditions, generated within a $3 \times 3 \times 1$ m box of the 3D space. To easily compare the effect of different initial and final configurations, we have fixed point C at the origin and generated four test cases for A and F (the initial quadrotor position relative to the load position, and the target load position). Simulations show that smooth trajectories can be generated using the proposed method to rapidly grasp the payload, take it to the target location, and release it. It can be seen in Fig. 5 that often maximal accelerations are required, which shows optimality of the solutions, as the system is operated at the limits.

C. Control performance

We study the performance of the robust geometric controller by comparing it to the original version of geometric control proposed in [18] to show the importance of the robustness in the payload transportation scenario. We evaluate the performance of the methods using the control gains given in Table 1, and by applying external disturbance to the manipulator, characterized by:

$$F_{\text{ext}} = [0.1 \ 0.1 \ 0]^T \text{ N}. \quad (27)$$

In real-world applications, such a constant force disturbance can occur due to wind. We set the disturbance magnitude terms of the robust control inputs in (20) to bound the norm of F_{ext} , as follows:

$$\delta_r = 0.3 \text{ N}, \quad \delta_R = 0. \quad (28)$$

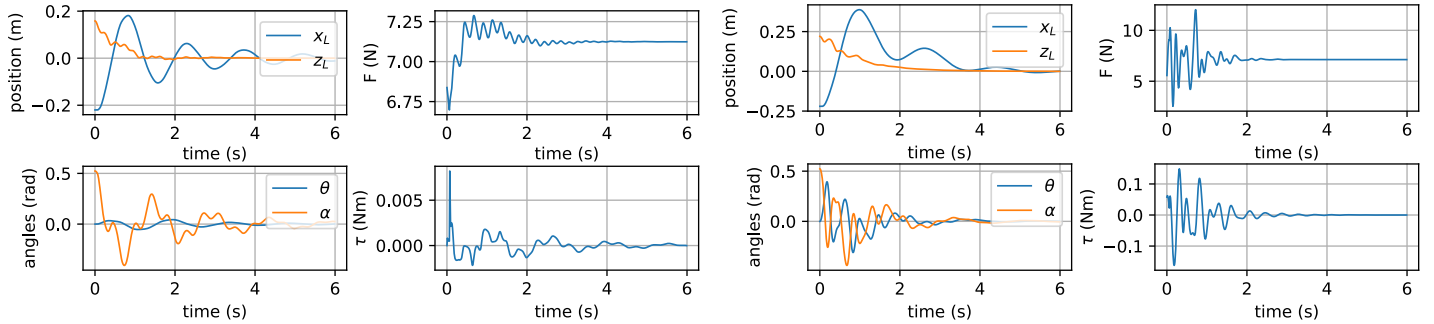


Fig. 6: Payload stabilization: closed loop response of the geometric control (left), and the LQ payload regulator (right).

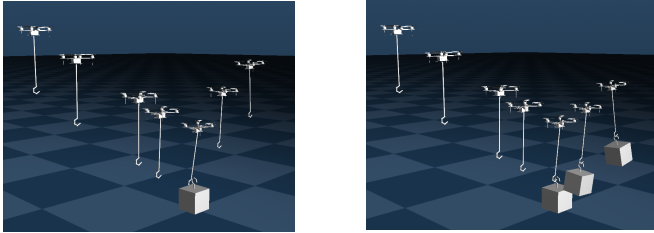
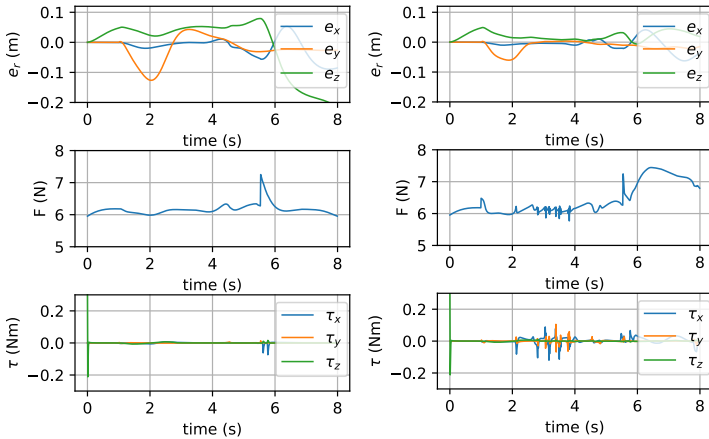


Fig. 7: Payload grasping in the presence of external wind disturbance using the geometric controller of [18] (left), and the introduced robust geometric controller (right). The trajectory tracking error (e_r), the control inputs (F, τ), and composite images from the MuJoCo simulation are shown. The reference trajectory tracked by the controllers is displayed in the rightmost plot of Fig. 5.

The simulation results are shown in Fig. 7, where the controller is tracking the rightmost trajectory of Fig. 5. On the left, it can be seen that the controller based on [18] cannot compensate the effect of the external disturbance, and the grasping is unsuccessful. However, the right plots show a successful grasping by the robust scheme. In the presence of the uncertainties, the position tracking errors (e_r) are significantly reduced by the robust controller, which is crucial to pick up the payload. The control input terms (F, τ) show a more aggressive regulation in case of the robust controller that is required for disturbance rejection. The performance of the grasping is shown by realistic simulation in MuJoCo, using the physical model of the manipulator.

Next, we examine the performance of the linear-quadratic payload regulator by stabilizing the swing of the payload at

point D . By substituting the physical parameters from Table 2 into (22), and solving the LQ optimization problem, we obtain the following linear feedback gain matrix:

$$K = \begin{bmatrix} 0 & 0 & 8.6 & 9.3 & 0 & 0 & 0 & 0 \\ 0.07 & 0.12 & 0 & 0 & 0.73 & 0.08 & -0.08 & 0.11 \end{bmatrix}.$$

The closed loop response by the LQR compared to the robust geometric controller is displayed in Fig. 6, using the following initial condition:

$$\xi(0) = [-0.217 \ 0 \ 0.140 \ 0 \ 0 \ 0 \ \frac{\pi}{6} \ 0]^T. \quad (29)$$

Our results show that using the LQR controller, the system is stable around the operating point and all states converge to zero in less than 4 seconds, despite the fact that K has been designed based on a linearized model of the full system dynamics. In contrast, without using the stabilizing LQR controller, damping of the oscillations of the payload is significantly slower.

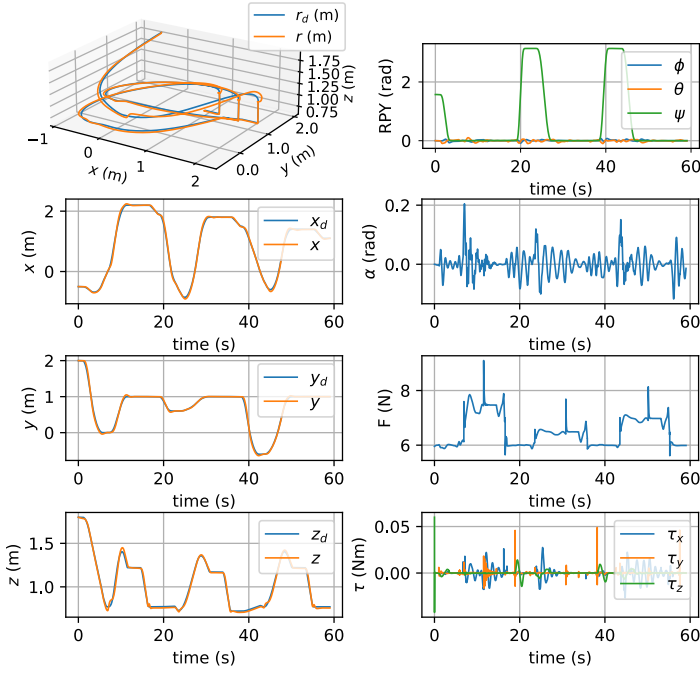
D. Test scenario for transporting multiple payloads

To challenge the proposed methods, we have constructed a real-world scenario, corresponding to the sequential transportation of three payloads with different sizes and masses. All three objects are cuboids, with the following parameters:

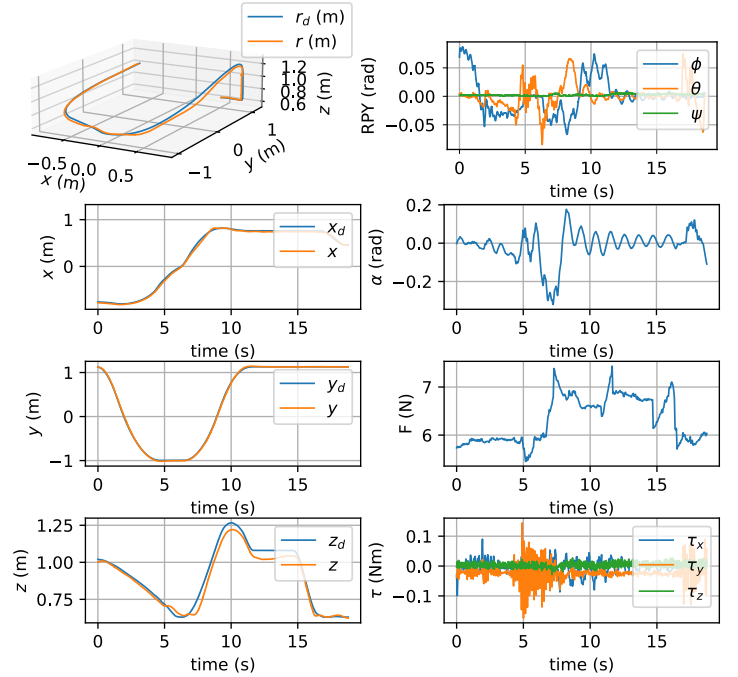
$$\begin{aligned} w_1 &= 10 \text{ cm}, & h_1 &= 10 \text{ cm}, & m_1 &= 0.15 \text{ kg}, \\ w_2 &= 7.5 \text{ cm}, & h_2 &= 7.5 \text{ cm}, & m_2 &= 0.05 \text{ kg}, \\ w_3 &= 7.5 \text{ cm}, & h_3 &= 10 \text{ cm}, & m_3 &= 0.1 \text{ kg}, \end{aligned} \quad (30)$$

where w is the width (both in x and y directions), h is the height, and m is the mass of each payload. The inertia of each payload is determined by MuJoCo based on their geometry and mass.

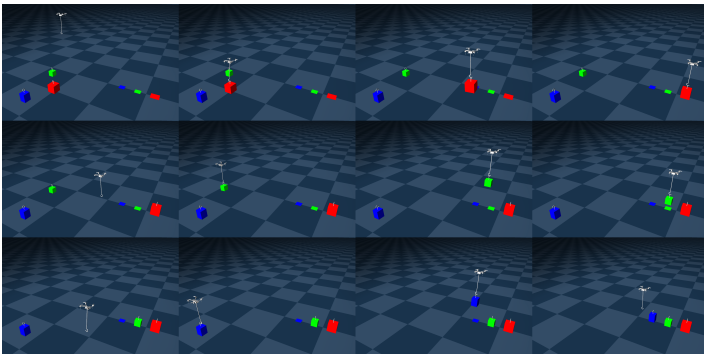
The result of the test scenario is illustrated in Fig. 8. The composite image containing snapshots from the MuJoCo simulation makes it easier to understand the plot of the reference tracking and the transportation sequence can be easily followed. The first payload is depicted by red color, the second is green, and the third is blue. The target location of each payload is also visualized by a plane with matching color. The upper plot shows the reference trajectory of the quadrotor together with the simulation result. The root mean square error of the position tracking is $e_{r, \text{RMSE}} = 4.932$ cm, and the maximum value is $\|e_r\|_{\max} = 12.4$ cm, showing high performance



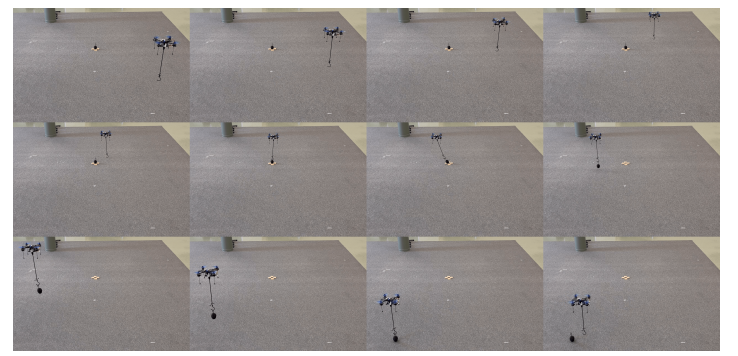
(a) Quadrotor position (x, y, z) , swing angle (α) , and inputs (F, τ) .



(a) Quadrotor position (x, y, z) , swing angle (α) , and inputs (F, τ) .



(b) Composite image of the MuJoCo simulation.



(b) Composite image of the flight experiment.

Fig. 8: Sequential transportation of three payloads with different shape and mass in simulation.

of the applied control scheme. The final position errors of the three payloads are as follows:

$$\begin{bmatrix} e_x \\ e_y \end{bmatrix} = \left\{ \begin{bmatrix} -0.7 \\ 0.65 \end{bmatrix}, \begin{bmatrix} 0.3 \\ -0.022 \end{bmatrix}, \begin{bmatrix} 0.77 \\ -0.35 \end{bmatrix} \right\} \text{ mm}, \quad (31)$$

all of which are below one millimeter. The high precision of the payload release is due to the LQR payload stabilizing controller that is activated at point D of each trajectory for 3 seconds. The trajectory of the swing angle α is depicted in Fig. 8a, showing a maximum of 0.2045 rad that appears at the grasping point of the first payload with the highest mass. After attaching the hook, the swing of each payload becomes significant, however, the robust controller and the LQR are able to damp the oscillations to achieve precise positioning and high performance transportation.

Fig. 9: Real-world experiment of the payload transportation.

VI. REAL-WORLD EXPERIMENTS

Flight experiments have been conducted with the proposed method, implemented on a self-developed quadrotor platform equipped with a 3D printed hook and revolute joint, shown in Fig. 1. The on-board computation runs on a Crazyflie Bolt flight controller, including an IMU and two microcontroller units. Optitrack motion capture system is used to provide high precision pose information. A more detailed specification of the experimental setup is available in [19]. The physical parameters of the hook-based manipulator are shown in Table 2, and for the flight experiments, we use a payload with mass $m_L = 63$ g.

Measurement results of the flight experiment are displayed in Fig. 9. The upper plot shows the position reference and measurement during the maneuver. The root mean square error of the position tracking is $e_{r,\text{RMSE}} = 4.58$ cm, and the maximum error is $\|e_r\|_{\text{max}} = 11.4$ cm, which are even lower

than the values obtained in simulation. The final position error of the payload is $[e_x, e_y] = [21.1, 1.2]$ mm, showing that the control scheme performs very well in real-world deployment. The absolute maximum of the swing angle α is 0.32 rad that is 50% higher than the maximum value obtained in simulation, however, the control system is able to damp the oscillations in real flights, as well, to achieve precise positioning at the release of the payload.

It is important to note that unmodeled aerodynamics, more specifically drag, downwash and ground effect have a significant impact on the behaviour of the system in real flight experiments, see [16, 20]. For flat and light objects that have large aerodynamic resistance, the wind generated by the propellers can cause the payload to swing on the hook, which can be challenging to compensate by the controller. Therefore the modelling of this aerodynamic effect and integration in the control design is an important task of the future research.

To illustrate the main results of this work, a video is available at <https://youtu.be/VEVNBuLufE3M>.

VII. CONCLUSION

In this work, we have presented a complete methodology for payload grasping, transportation, and release using a quadrotor with a hook-based manipulator. To validate the proposed method, first we have implemented the corresponding motion planning and control algorithms in a high-fidelity physical simulator. To test the real-world applicability of our solution, we have also deployed the algorithms on a hardware platform and performed flight experiments. The demonstrated results show that the proposed trajectory planning and control methods are time efficient, robust, and can be applied in real flights. However, there is still room for improvement (e.g. aerodynamic modelling) to be ready for industrial application.

REFERENCES

- [1] O. Maghazei and T. Netland, "Drones in manufacturing: Exploring opportunities for research and practice," *Journal of Manufacturing Technology Management*, vol. 31, no. 1, pp. 1237–1259, 2020.
- [2] M. Gassner, T. Cieslewski, and D. Scaramuzza, "Dynamic collaboration without communication: Vision-based cable-suspended load transport with two quadrotors," in *Proc. of the IEEE International Conference on Robotics and Automation*. Institute of Electrical and Electronics Engineers Inc., 2017, pp. 5196–5202.
- [3] H. Hua, Y. Fang, X. Zhang, and C. Qian, "A time-optimal trajectory planning strategy for an aircraft with a suspended payload via optimization and learning approaches," *IEEE Transactions on Control Systems Technology*, pp. 1–11, 2021.
- [4] K. Sreenath, N. Michael, and V. Kumar, "Trajectory generation and control of a quadrotor with a cable-suspended load - a differentially-flat hybrid system," in *Proc. of the IEEE International Conference on Robotics and Automation*, 2013, pp. 4888–4895.
- [5] K. Sreenath and V. Kumar, "Dynamics, control and planning for cooperative manipulation of payloads suspended by cables from multiple quadrotor robots," in *Proc. of the Robotics: Science and Systems*, 2013.
- [6] A. Ollero, M. Tognon, A. Suarez, D. Lee, and A. Franchi, "Past, present, and future of aerial robotic manipulators," *IEEE Transactions on Robotics*, vol. 38, no. 1, pp. 626–645, 2022.
- [7] V. Lippiello and F. Ruggiero, "Cartesian impedance control of a UAV with a robotic arm," in *Proc. of the 10th International IFAC Symposium on Robot Control*, vol. 45, 2012, pp. 704–709.
- [8] J. Thomas, G. Loianno, J. Polin, K. Sreenath, and V. Kumar, "Toward autonomous avian-inspired grasping for micro aerial vehicles," *Bioinspiration and Biomimetics*, vol. 9, no. 2, 2014.
- [9] F. Augugliaro, S. Lupashin, M. Hamer, C. Male, M. Hehn, M. W. Mueller, J. S. Willmann, F. Gramazio, M. Kohler, and R. D'Andrea, "The flight assembled architecture installation: Cooperative construction with flying machines," *IEEE Control Systems Magazine*, vol. 34, no. 4, pp. 46–64, 2014.
- [10] D. Verscheure, B. Demeulenaere, J. Swevers, J. D. Schutter, and M. Diehl, "Time-optimal path tracking for robots: A convex optimization approach," *IEEE Transactions on Automatic Control*, vol. 54, pp. 2318–2327, 2009.
- [11] T. Lee, M. Leok, and N. H. McClamroch, "Nonlinear robust tracking control of a quadrotor UAV on SE(3)," *Asian Journal of Control*, vol. 15, pp. 391–408, 2013.
- [12] E. Todorov, T. Erez, and Y. Tassa, "Mujoco: A physics engine for model-based control," in *IEEE/RSJ International Conference on Intelligent Robots and Systems*, 2012, pp. 5026–5033.
- [13] D. Mellinger and V. Kumar, "Minimum snap trajectory generation and control for quadrotors," in *Proc. of the IEEE International Conference on Robotics and Automation*. IEEE, 2011, pp. 2520–2525.
- [14] F. Gao, W. Wu, J. Pan, B. Zhou, and S. Shen, "Optimal time allocation for quadrotor trajectory generation," in *Proc. of the IEEE/RSJ International Conference on Intelligent Robots and Systems*, 2018, pp. 4715–4722.
- [15] S. LaValle, M. Branicky, and S. Lindemann, "On the relationship between classical grid search and probabilistic roadmaps," *The International Journal of Robotics Research*, vol. 23, no. 7-8, pp. 673–692, 2004.
- [16] L. Bauersfeld, E. Kaufmann, P. Foehn, S. Sun, and D. Scaramuzza, "Neurobem: Hybrid aerodynamic quadrotor model," in *Proc. of the Robotics: Science and Systems*, 2021.
- [17] H. Kwakernaak and R. Sivan, *Linear optimal control systems*. New York: Wiley Interscience, 1972.
- [18] T. Lee, M. Leok, and N. H. McClamroch, "Geometric tracking control of a quadrotor UAV on SE(3)," in *Proc. of the 49th IEEE Conference on Decision and Control*, 2010, pp. 5420–5425.
- [19] P. Antal, T. Péni, and R. Tóth, "Backflipping with miniature quadcopters by Gaussian Process based control and planning," *submitted to IEEE Transactions on Control Systems Technology*, 2022, <https://arxiv.org/abs/2209.14652>.
- [20] C. Powers, D. Mellinger, A. Kushleyev, B. Kothmann, and V. Kumar, *Influence of Aerodynamics and Proximity Effects in Quadrotor Flight*. Heidelberg: Springer International Publishing, 2013, pp. 289–302.